

Thermodynamic Assessment of the Solar-to-fuel Performance of
La_{0.6}Sr_{0.4}Mn_{1-y}Cr_yO_{3-δ} Perovskite Solid Solution Series

Alexander H. Bork^{a,b,c}, Erwin Povoden-Karadeniz^d, Alfonso J. Carrillo^{a,b,c}, Jennifer L.M. Rupp^{a,b,c}

- (a) Electrochemical Materials, Department of Materials Science, ETH Zurich, Hönggerberggring 64,8093 Zürich, Switzerland
- (b) Electrochemical Materials Laboratory, Department of Materials Science and Engineering, Massachusetts Institute of Technology, Cambridge, MA, USA
- (c) Electrochemical Materials Laboratory, Department of Electrical Engineering and Computer Science, Massachusetts Institute of Technology, Cambridge, MA, USA
- (d) Christian-Doppler Laboratory Interfaces and Precipitation Engineering CDL-IPE, Institute of Materials Science and Technology, TU Wien, Vienna, Austria

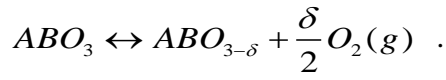
Abstract

In the search of new materials for the solar-to-fuel technology, we turn to the material class of perovskites that offer wide possibilities in manipulation of its chemistry and catalytic activity. Here, we access the role of Cr in the $\text{La}_{0.6}\text{Sr}_{0.4}\text{Mn}_{1-y}\text{Cr}_y\text{O}_{3-\delta}$ perovskite solid solution hitherto unexplored for two-step solar thermochemical fuel production. A multi-component Calphad defect model for the system La-Sr-Cr-Mn-O is therefore optimized and used for computations of oxygen nonstoichiometries and redox thermodynamics of the $\text{La}_{0.6}\text{Sr}_{0.4}\text{Mn}_{1-y}\text{Cr}_y\text{O}_{3-\delta}$ solution series in the temperature range of 1073 to 1873 K as a potential operation window for solar-to-fuel conversion. Modeling results reveal two advantages of substituting manganese by chromium. Firstly, it is possible to reduce the heat capacity with up to 10%, to a value of $132 \text{ J mol}^{-1} \text{ K}^{-1}$. Secondly, the thermodynamic driving force for solar-to-fuel conversion increases and the Cr-doped materials provide higher yield and efficiency at isothermal operation. The proposed model allows for continuous simulative scanning of redox thermodynamics from zero Cr-doping to a fully substituted chromite perovskite. For isothermal water splitting, the composition $\text{La}_{0.6}\text{Sr}_{0.4}\text{Mn}_{0.2}\text{Cr}_{0.8}\text{O}_{3-\delta}$ displays the highest fuel yield and efficiency of 2.7% due to a high thermodynamic driving force at elevated temperature for this composition. These predictive insights give prospects for engineering the thermodynamics of the oxygen release reaction in perovskites towards higher fuel production and efficiency in solar-to-fuel reactors with isothermal operation.

Keywords: solar-to-fuel, thermochemical cycling, chromium doped lanthanum strontium manganite, perovskite, defect modeling

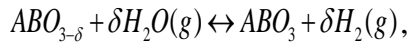
1 Introduction

Solar-driven thermochemical dissociation of CO₂ and H₂O to syngas presents an attractive avenue away from dependence on fossil fuels[1; 2]. Intermittent solar energy may be stored in chemical fuels and distributed on demand for transportation whilst mitigating CO₂ emissions. The working principle of two-step solar thermochemical fuel production may be exemplified by the changes in the oxygen nonstoichiometry, δ , of a perovskite with the general structure ABO_{3- δ} . In the first step, at a temperature of 1350°C the perovskite oxide is reduced by solar thermal energy [3-6] and oxygen is released

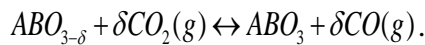


Eq. 1

Through a second step, the perovskite is oxidized in the presence of H₂O and CO₂, thus producing hydrogen and carbon monoxide (syngas) at a temperature of 1000°C through the following reactions:



Eq. 2a



Eq. 2b

The produced syngas (H₂ + CO) in a solar thermochemical reactor may be converted into hydrocarbon fuels by commercial Fischer-Tropsch process [7]. Nowadays researchers aim at finding new efficient and stable materials to perform thermochemical water and carbon dioxide splitting. Perovskites have received significant attention due to high fuel production [3; 4; 8-13]. McDaniel *et al.* [3] revealed that (La,Sr)MnO₃ perovskites doped with Al on the B-site produced 9 times more H₂ and 6 times more CO compared to state-of-the-art material, ceria, when reduced at 1350°C and oxidized at 1000 °C. Despite the promising

1 results, thermodynamic analysis based on thermogravimetric experiments have shown that
2 perovskites of $\text{La}_{1-x}\text{Sr}_x\text{Mn}_{1-y}\text{Al}_y\text{O}_{3-\delta}$ have a lower mass specific fuel productivity and
3 efficiency compared to ceria [6; 14-17]. The lower efficiency is due to a high heat capacity
4 and in particular a low absolute value of the Gibbs energy change of oxygen vacancy
5 formation.
6
7
8
9

10
11 This work employs thermodynamic computation to make a predictive investigation of the
12 multicomponent perovskite $\text{La}_{0.6}\text{Sr}_{0.4}\text{Mn}_{1-x}\text{Cr}_x\text{O}_3$ as a new candidate for the solar-to-fuel
13 application. Chromium is added to the B-site of the ABO_3 perovskite with the incentive to
14 increase Gibbs energy change of oxygen formation and lower the heat capacity to fulfill the
15 requirements for a higher efficiency. We ensure a single-phase and chemically stable
16 perovskite utilizing a strontium content of 0.4 on the A-site [4; 18] and systematically alter
17 the ratio between chromium and manganese on the B-site. Recently, we presented and
18 verified a new approach using computational thermodynamics with an optimized Calphad
19 defect model of the perovskite $\text{La}_{1-x}\text{Sr}_x\text{MnO}_3$ [17; 19]. Here, we propose an optimal
20 composition of an extended perovskite with two A-site (La,Sr) and two B-site (Mn,Cr)
21 dopants for improved efficiency of two-step solar thermochemical fuel production by
22 thermodynamic and defect chemistry computation. The evaluation will be used to examine
23 the trade-off between oxygen release, heat capacity, and favorability for water splitting to
24 hydrogen and analyze the implications on the efficiency. The analysis is carried out for
25 conventional two-step cycling with reduction at 1773K and oxidation temperature at 1073K.
26 Furthermore, we study the effect of increasing the oxidation temperature towards isothermal
27 operation at 1773K. This is motivated by recent experimental findings showing superior
28 performance of $\text{La}_{1-x}\text{Sr}_x\text{MnO}_{3-\delta}$ compared to state-of-the-art material ceria at isothermal
29 conditions [20]. Furthermore, isothermal operation may simplify the reactor design with less
30 stress on the active and containing materials and alleviate the need for solid-solid heat
31 recuperation [13; 21].
32
33
34
35
36
37
38
39
40
41
42
43
44
45
46
47
48
49
50
51
52
53
54
55
56
57
58
59
60
61
62
63
64
65

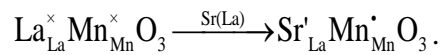
2 Modeling approach

For the modeling approach utilized in this work, it is important to distinguish between the *thermodynamics of the perovskite phase* formation, being represented by its Gibbs energy, and the *thermodynamics of the oxygen release reaction*. In essence, the Calphad approach is used to determine the equilibrium thermodynamics of the perovskite phase, which relies on an optimization towards the available experimental data. Since reduced compounds are also defined in the Calphad model of the perovskite phase, defect chemistry can also be simulated, aside of its molar enthalpy, entropy and heat capacity.

From the Calphad model of oxygen nonstoichiometry, we are able to derive the thermodynamics of the oxygen release reaction, which contains the Gibbs free energy, enthalpy and entropy of the oxygen release reaction. Using those parameters it is possible make a successful thermodynamic assessment including the materials' fuel production and efficiency [17].

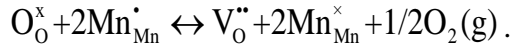
2.1 Defect chemistry model of $\text{La}_{1-x}\text{Sr}_x\text{Mn}_{1-y}\text{Cr}_y\text{O}_{3-\delta}$

In the Calphad model of $\text{La}_{1-x}\text{Sr}_x\text{Mn}_{1-y}\text{Cr}_y\text{O}_{3-\delta}$ perovskite [22], which is represented by the formula $[\text{La}^{3+}, \text{Sr}^{2+}]^{\text{A}}[\text{Mn}^{2+}, \text{Mn}^{3+}, \text{Mn}^{4+}, \text{Cr}^{3+}, \text{Cr}^{4+}]^{\text{B}}[\text{O}^{2-}, \text{Va}^0]_3$, the solution of Sr^{2+} on La^{3+} sites in $\text{La}_{1-x}\text{Sr}_x\text{Mn}_{1-y}\text{Cr}_y\text{O}_{3-\delta}$ results in charge deficiency, which (in air) is mainly compensated by oxidation of either $\text{Mn}^{3+}/\text{Mn}^{4+}$ or $\text{Cr}^{3+}/\text{Cr}^{4+}$. In Kröger-Vink notation this can be expressed for changes in Mn as

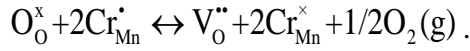


Eq. 3 Here, $\text{La}_{\text{La}}^{\times}$ signifies a lanthanum ion on lanthanum site with neutral charge, while Sr'_{La} indicates a strontium ion on a lanthanum site with a single negative charge, and $\text{Mn}_{\text{Mn}}^{\bullet}$ is a manganese ion at the B-site ABO_3 perovskite lattice with a single positive charge. The

mechanism for reduction is change of the oxidation state of the B-site cation, followed by formation of oxygen vacancy ($V_O^{\bullet\bullet}$) defect according to



Eq. 4a



Eq. 4b

In fact, it has been shown experimentally that manganese on the perovskite B-site is more prone to oxidation state changes compared to chromium for lower Sr contents of $x < 0.3$ in $La_{1-x}Sr_xMn_{0.5}Cr_{0.5}O_{3-\delta}$ [23; 24]. However, defect evolution of the end-member $La_{1-x}Sr_xCrO_{3-\delta}$ compound of the perovskite solid solution also involves Cr^{4+} , aside of oxygen vacancies [25]. Moreover, we consider high strontium contents of $x = 0.4$ on the A-site and high chromium concentrations of up to $y = 0.9$, so also chromium will change oxidation state to maintain charge neutrality. Therefore, we include Cr^{4+} in the model as well.

2.2 Thermodynamic modeling of perovskite solution phase using reciprocal compound energy relations

The thermodynamics of a multi-component perovskite oxide solid solution is comprised of the stoichiometrically weighted sum of Gibbs energy functions of ternary perovskite compounds ABO_3 . Its general form being presented in Eq. 5

$$\begin{aligned} {}^{\circ}G_m^{prv} &= \sum_i \sum_j \sum_k y_i y_j y_k {}^{\circ}G_{i,j,k} + \frac{I}{\sum_s n^{(s)}} RT \sum_s \sum_i n^{(s)} y_i^{(s)} \ln y_i^{(s)} + E G_m^{prv}, \\ E G_m^{prv} &= \sum_s \sum_i \sum_j y_i^{(s)} y_j^{(s)} \sum_{r \neq s} \sum_k y_k^{(r)} L_{i,j,\dots,k} \end{aligned}$$

Eq. 5

where y_i is the site fraction of each cation on the A-sublattice, y_j is the site fraction of each cation on the B-sublattice, and y_k is the site fraction of O^{2-} and Va on the anion sublattice.

$R=8.31451 \text{ Jmol}^{-1}\text{K}^{-1}$, $n^{(s)}$ are stoichiometric coefficients relating the sublattices. The second-last term accounts for the configurational entropy of mixing. The last term E_m^{prv} describes the excess, non-ideal Gibbs interaction energy of mixing of different species on one sublattice. In the present perovskite description, simultaneous interactions of ions on A- and B-sublattices of the perovskite phase are represented by the last term of Eq. 5. The parameters of the compound energy formalism are the stoichiometrically weighted Gibbs energies of the end-member compounds ${}^\circ G_{i,j,k}$.

In terms of optimizable parameter description, ${}^\circ G_{i,j,k}$ can be represented by a Gibbs energy polynomial. An ABO_3 perovskite line compound phase is simply written as

$$G_m^{\text{ABO}_3} = a + bT + cT \ln T + dT^2 + eT^3 + fT^{-1},$$

Eq. 6

and, since

$$\Delta H = \Delta G + TS = a - cT - dT^2 - 2eT^3 + 2fT^{-1},$$

Eq. 7

one obtains an equation for the heat capacity

$$C_p^{\text{prv}} = \left(\frac{\partial H}{\partial T} \right) = T \left(\frac{\partial S}{\partial T} \right) = -c - 2dT - 6eT^2 - 2fT^{-2}.$$

Eq. 8

Model parameters c, d, e, f in Eq. 8 are adjusted by experimental heat capacities, whereas a and b (Eq. 6) are related to enthalpy and entropy, respectively. Heat capacities of multi-component perovskite are, as a reasonable approximation of negligible “non-ideal” heat capacity contributions, simply defined by Neumann Kopp’s rule [27], i.e. stoichiometrically and charge-balanced weighted sum of compound heat capacities.

Describing a continuous Gibbs energy of a perovskite solid solution from oxidized to reduced conditions requires stoichiometrically proper summing up of end-member compounds, obeying charge neutrality. In fact, the present multi-component perovskite sublattice formula $[La^{3+}, Sr^{2+}]^A[Mn^{2+}, Mn^{3+}, Mn^{4+}, Cr^{3+}, Cr^{4+}]^B[O^{2-}, Va^0]_3$ delivers (by simple recombination: ABO_3 , $ABVa_3$ compounds) 20 end-member compounds, with only two of them showing charge-neutrality, as illustrated by the simple geometric representation of the perovskite phase, Figure 1. Neutral compounds of the La-Sr-Cr-Mn oxide perovskite solid solution span the charge neutrality plane, which represents potentially realized mixed-valence perovskite in the scope of changing redox conditions. Two corner compositions of the neutral plane, $Sr_2O_{2/3}Va_{1/3}$ and $Lr_2O_{5/6}Va_{1/6}$ are defined by combinations of charged perovskite end-member compounds, e.g. Sr_2O represents $Sr^{2+}Mn^{2+}(O^{2-})_3$. Realization of physically meaningful parametrization of 20 compound energies, most of them being charged, is indeed arguable. An appropriate diminution of parameters is obtained by the following considerations on reciprocal relations among end-member compounds.

For a general 4-component solution phase $(A,B)(C,D)$, the reciprocal system of compound $A:B$, $A:D$, $B:C$, $B:D$ Gibbs energies can be set up as these end-members representing the corners of a simple “composition square”. According to Hillert [26], a solution phase with composition $(A_{0.25}B_{0.25})(C_{0.25}D_{0.25})$, i.e. lying in the center of the square will tend to decompose to either $(A:C)$ and $(B:D)$ compounds or $(A:D)$ and $(B:C)$ compounds. The driving force of this de-mixing is defined by the reciprocal reaction parameter,

$$^{\circ}Gr = ^{\circ}G(A:D) + ^{\circ}G(B:C) - ^{\circ}G(A:C) - ^{\circ}G(B:D).$$

Eq. 9

The present case multi-component perovskite consists of a number of reciprocal systems, such as $LrO-LrV-SrO-SrV$ in Fig. 1. Reciprocal systems of the perovskite phase, as represented by each of the square faces of the composition body, Figure 1, comprise mostly charged and thus purely virtual corner compounds. Since the charged compounds are

unlikely to form it is a reasonable and a successful modelling strategy to set $^{\circ}\text{Gr}$ equal to zero [21]. Setting the sum of this term to zero sets a useful constraint on the interaction energy parameters.

By the reciprocal relations approach, the thermodynamics of the whole perovskite solid solution is defined, still accepting ideal mixing among species in one sublattice. Whether this assumption is legitimate, is directly revealed by comparison of experimental defect chemistry data with the modeling results. In the present case of $\text{La}_{1-x}\text{Sr}_x\text{Mn}_{1-y}\text{Cr}_y\text{O}_{3-\delta}$ perovskite, interactions representing non-ideal mixing among Cr^{3+} and Mn^{3+} or Mn^{4+} are introduced in the model, since an offset between experimental oxygen nonstoichiometries and modeling results was found by ideal model extension from quaternary subsystems to quinternary La-Sr-Cr-Mn-O. For the fitting procedure of these interaction energies, $L_{i,j,\dots,k}$ in Eq. 5, we use Redlich-Kister [27] polynomials.

$$L_{La+3,Sr+2:Cr+3,Mn+3:O-2} = \sum_{k=0}^2 L_{La+3,Sr+2:Cr+3,Mn+3:O-2} (y_{La+3} - y_{Sr+2})^k (y_{Cr+3} - y_{Mn+3})^k ,$$

Eq. 10

and

$$L_{La+3,Sr+2:Cr+3,Mn+4:O-2} = \sum_{k=0}^2 L_{La+3,Sr+2:Cr+3,Mn+4:O-2} (y_{La+3} - y_{Sr+2})^k (y_{Cr+3} - y_{Mn+4})^k$$

Eq. 11

The coefficients k (0^{th} , 1^{st} , 2^{nd} order) act on composition-dependent Gibbs energies differently and are chosen to give the best fit to the available experimental data of compositions with both Cr and Mn on the B-site.

2.3 Thermodynamics of the oxygen release reaction

According to Panlener et al [28], the partial molar enthalpy (Δh) and partial molar entropy (Δs) of the oxygen release reaction are related to the oxygen nonstoichiometry, δ , and oxygen partial pressure, pO_2 by the following relations in Eq. 12 and Eq. 13.

$$\frac{1}{2}RT \ln pO_2 = \Delta h_{\text{red}} - T\Delta s_{\text{red}}$$

Eq. 12

$$\frac{1}{2} \ln pO_2 = \frac{\Delta h_{\text{red}}}{RT} - \frac{\Delta s}{R} \bigg|_{\delta=\text{constant}}$$

Eq. 13

Thus, for constant δ the thermodynamic entities may be derived from the slope and intercept in a plot of oxygen partial pressure and the reciprocal temperature $1/T$ [17; 19; 29].

3 Results and Discussion

3.1 Comparison of predicted and experimental oxygen nonstoichiometry of $\text{La}_{0.75}\text{Sr}_{0.25}\text{Mn}_{0.5}\text{Cr}_{0.5}\text{O}_{3-\delta}$

The results of the Calphad defect model are compared to experimental data on oxygen nonstoichiometry, δ , as function of oxygen partial pressure for the composition in $\text{La}_{0.75}\text{Sr}_{0.25}\text{Mn}_{0.5}\text{Cr}_{0.5}\text{O}_{3-\delta}$ in the temperature range 973K to 1273K see Figure 2. A strong agreement is observed for this perovskite with an equal amount of Cr and Mn on the B-site. Since the model is likewise able to reproduce and predict variations of A-site composition in the end-member compositions, i.e. $\text{La}_{1-x}\text{Sr}_x\text{CrO}_3$ and $\text{La}_{1-x}\text{Sr}_x\text{MnO}_3$ consistently, we conclude that the chosen model parameters provide the best representation of defect chemistry of the $\text{La}_{1-x}\text{Sr}_x\text{Mn}_{1-y}\text{Cr}_y\text{O}_{3-\delta}$ perovskite oxide. All tests of alternative parameterizations required considerably higher (and presumably unlikely) excess energies for a comparable agreement between calculated and experimental nonstoichiometries, or the same agreement could not be reached at all. The chosen Redlich-Kister parameters

accounting for non-ideal interactions between Cr- and Mn-valencies on the B-sites are listed in Table 1. For the purpose of reproducing our computations with the Thermocalc software package, we provide the complete set of thermodynamic parameters in Supporting Information Table 2 in a database format [30].

3.2 Computed of oxygen nonstoichiometry of $\text{La}_{0.6}\text{Sr}_{0.4}\text{Mn}_{1-y}\text{Cr}_y\text{O}_{3-\delta}$ perovskite oxide

Computed oxygen nonstoichiometry data are depicted in a temperature window of 1073-1873K relevant for classic solar-to-fuel reactors in Figure 3. We show the nonstoichiometry as function of oxygen partial pressure for four different chromium doping concentrations $y = 0, 0.2, 0.5$ and 0.9 for $\text{La}_{0.6}\text{Sr}_{0.4}\text{Mn}_{1-y}\text{Cr}_y\text{O}_{3-\delta}$, in Figures 3a-d respectively. For all compositions, an increased oxygen release for higher temperatures and lower oxygen partial pressure is obtained. The evaluation reveals that the values are strongly dependent on the B-site doping with chromium and that the oxygen release profiles shift towards lower $p\text{O}_2$ for higher chromium content. Comparing for example at the highest temperature 1873 K, the composition $\text{La}_{0.6}\text{Sr}_{0.4}\text{MnO}_{3-\delta}$ reaches an oxygen nonstoichiometry of $\delta = 0.2$ at an oxygen partial pressure of $p\text{O}_2 = 10^{-5.6}$ atm. In order to reach the same oxygen nonstoichiometry for a doping content of $y = 0.2, 0.5$ and 0.9 at 1873 K, the oxygen partial pressure is equal to $10^{-6.7}$ atm, $10^{-8.4}$ atm, $10^{-13.4}$ atm, correspondingly. For comparison of oxygen nonstoichiometry as function of temperature at fixed oxygen partial pressure, see Supporting Information S1.

3.3 Heat capacity of the perovskite type oxide $\text{La}_{0.6}\text{Sr}_{0.4}\text{Mn}_{1-y}\text{Cr}_y\text{O}_{3-\delta}$ by thermodynamic computation

Materials with a low heat capacity are in general desirable for the solar-to-fuel technology because the energy penalty for heating the material is lower and the efficiency thus higher. In Figure 4, we plot modeled heat capacity, from Eq. 8, as function of temperature for solid solutions of $\text{La}_{0.6}\text{Sr}_{0.4}\text{Mn}_{1-y}\text{Cr}_y\text{O}_{3-\delta}$ with respect to chromium concentration in the entire solid solution range from $y = 0.0$ -1.0. The heat capacity is plotted at a typical oxygen partial

pressure for solar-to-fuel reactors of 10^{-6} atm. in the temperature range from 1173 K to 1873 K. It is noted, that the heat capacity increases as function of temperature for all compositions and most interestingly, it decreases for higher chromium content. We find that increasing the chromium content from $y = 0$ to a value of $y = 1.0$, decreases the heat capacity by 10% from $147 \text{ J mol}^{-1} \text{ K}^{-1}$ to a value of $132 \text{ J mol}^{-1} \text{ K}^{-1}$ at 1173 K. For perspective, the benchmark material ceria has a heat capacity that has a lower value of $80 \text{ J mol}^{-1} \text{ K}^{-1}$. [31]

3.4 Calculated thermodynamics of the oxygen release reaction as function of oxygen nonstoichiometry for $\text{La}_{0.6}\text{Sr}_{0.4}\text{Mn}_{1-y}\text{Cr}_y\text{O}_{3-\delta}$

The partial molar enthalpy and entropy of the oxygen release reaction derived from the oxygen nonstoichiometry are presented in Figure 5. For increasing oxygen release most compositions of $\text{La}_{0.6}\text{Sr}_{0.4}\text{Mn}_{1-y}\text{Cr}_y\text{O}_{3-\delta}$ display an increase in enthalpy, whereas there is a decrease in entropy as function of oxygen release, Figure 5a and 5b. In Figure 5c, we show the Gibbs free energy change of reduction of the perovskites $\text{La}_{0.6}\text{Sr}_{0.4}\text{Mn}_{1-y}\text{Cr}_y\text{O}_{3-\delta}$ from the enthalpy and entropy as function of temperature. Importantly, this figure shows that Cr-doping results in a higher value of Δg_{red} , *i.e.* more energy is required to reduce this perovskite solid solution. Equivalently, more energy is gained by oxidation. One can predict whether the metal oxide has favorable thermodynamics for solar-to-fuel conversion by analysing the Gibbs free energy change of the entire reaction given by

$$\Delta g_{\text{rxn}} = -\Delta g_{\text{red}} + \Delta g_{\text{H}_2\text{O}} .$$

Eq. 14

Where $\Delta g_{\text{H}_2\text{O}}$ is the Gibbs free energy change associated with water splitting. When the term Δg_{rxn} is negative, the perovskite is oxidized spontaneously in the presence of water. A similar expression can be written for CO_2 splitting, but the thermodynamics of this reaction is similar and equivalent conclusions can be made on the material performance, so it will not be considered here [15; 17]. As a result, it is observed that Cr-doping leads to more

favorable thermodynamics for water splitting because the total Gibbs free energy of the reaction Δg_{rxn} approaches negative values.

Most importantly, it is recognized from Figure 5c that $\text{La}_{0.6}\text{Sr}_{0.4}\text{MnO}_{3-\delta}$ has a steeper slope than $\text{La}_{0.6}\text{Sr}_{0.4}\text{CrO}_{3-\delta}$ of the Δg_{red} -function due to a large difference in the entropy. The difference in entropy has great consequences on the operation of the material, since a high value of Δg_{red} is desired for the gas splitting reaction. Considering $\text{La}_{0.6}\text{Sr}_{0.4}\text{MnO}_{3-\delta}$ for the sake of example, the Gibbs free energy of reduction, Δg_{red} , is 66 kJ mol^{-1} at a temperature 1873 K. For this material, it is necessary to lower the oxidation temperature to 1073 K to reach a value of 147 kJ mol^{-1} viz. it is operated best as conventional two-step metal oxide with reduction at high temperature and oxidation at a lower temperature in agreement with literature [6]. This behavior is in contrast to the material $\text{La}_{0.6}\text{Sr}_{0.4}\text{Mn}_{0.1}\text{Cr}_{0.9}\text{O}_{3-\delta}$ that shows a minor dependence on temperature and a high value of 170 kJ mol^{-1} at 1873 K. In other words, the Cr-doped material has a high thermodynamic driving force for water splitting even at high temperatures for isothermal conditions. See Supporting Information S2 for further insights on the relationship between the thermodynamics of the oxygen release reaction and Cr-doping.

3.5 Equilibrium hydrogen fuel yields of combined Cr- and Sr-doped lanthanum manganite produced by water splitting

Here, the effect of chromium doping on the B-site of $\text{La}_{0.6}\text{Sr}_{0.4}\text{Mn}_{1-y}\text{Cr}_y\text{O}_{3-\delta}$ on thermochemical water splitting is computed. In Figure 6, we focus on the hydrogen fuel yield of the $\text{La}_{0.6}\text{Sr}_{0.4}\text{Mn}_{1-y}\text{Cr}_y\text{O}_{3-\delta}$ perovskite-family as function of the water concentration. The hydrogen yields are plotted for an experiment with reduction at 1773 K and $p\text{O}_2 = 10^{-6}$ atm followed by oxidation at 1273 K. Applying these reducing conditions is motivated by previous thermochemical studies of the perovskite material $\text{La}_{0.6}\text{Sr}_{0.4}\text{MnO}_{3-\delta}$ at temperatures up to 1773 K [6; 15; 20] indicating that the materials remain chemically stable after cycling.

Substitution of manganese by chromium will further increase the chemical stability of the perovskite phase [23; 32].

From the plot in Figure 6, it is observed that the hydrogen yield of $\text{La}_{0.6}\text{Sr}_{0.4}\text{MnO}_{3-\delta}$ increases for higher water concentration and it reaches a plateau of 0.18 mol at a water concentration of $n_{\text{H}_2} = 10^4 n_{\text{ABO}_3}$ marked by the red dot. This means that this material will be re-oxidized completely, in a closed system by 10,000 moles of water per one mole of perovskite. Adding chromium to the B-site in $\text{La}_{0.6}\text{Sr}_{0.4}\text{Mn}_{1-y}\text{Cr}_y\text{O}_{3-\delta}$ results in considerably lower maximum fuel production yield, *e.g.*, $n_{\text{H}_2} = 0.03$ moles for $y = 0.9$. The low fuel production given for $y = 0.9$ is due to the low reduction extents, δ_{red} , at the given conditions of temperature and oxygen partial pressure. On the other hand, less water is required to fully oxidize the material in line with the increased thermodynamic driving force observed in Figure 3. For example, the material with the highest chromium content would be fully oxidized at a water concentration of $n_{\text{H}_2} = 10^{2.3} n_{\text{ABO}_3} \approx 200 n_{\text{ABO}_3}$

In this context, it is crucial to recognize all energetic inputs required to produce that fuel, for instance the energy penalty for heating water is directly proportional to the amount of water that is used in the reaction.

3.6 Optimized Cr-doping for improved efficiency of the thermochemical cycle

The performance of a material for the solar-to-fuel conversion process may be quantified by the thermal efficiency $\eta_{\text{solar-to-fuel}}$ [33; 34]

$$\eta_{\text{solar-to-fuel}} = \frac{\text{HHV}_{\text{H}_2} \times n_{\text{H}_2}}{Q_{\text{total}}}$$

Eq. 15

n_{H_2} is the hydrogen yield per mole perovskite per cycle, HHV_{H_2} is the higher heating value of hydrogen and Q_{total} is the total energy input required to produce that fuel. Here, we will set the energy penalties concerning reactor type to zero and focus on the relative

performance of the materials for different conditions, so the input energy $Q_{\text{solar,mat}}$ concerns the material specific properties required to drive the reaction [6; 17].

$$Q_{\text{solar,mat}} = \frac{1}{\eta_{\text{abs}}} \left(\Delta h_{\text{H}_2\text{O}|_{298\text{K} \rightarrow T_{\text{ox}}}} n_{\text{H}_2\text{O}} + \int_{T_{\text{ox}}}^{T_{\text{red}}} c_p dT + \Delta h_{\text{red}} \delta n_{\text{ox}} \right)$$

Eq. 16

Here, $\Delta h_{\text{H}_2\text{O}|_{298\text{K} \rightarrow T_{\text{ox}}}}$ is the energy required to heat the water from room temperature to the oxidation temperature, multiplied by $n_{\text{H}_2\text{O}}$ the moles of water per mole of perovskite.

$\int_{T_{\text{ox}}}^{T_{\text{red}}} c_p dT$ is the sensible heat of the metal oxide for the given temperature swing and Δh_{red} is the enthalpy change for the perovskite oxide for the number of moles of perovskite being reduced. The absorption efficiency is given by $\eta_{\text{abs}} = 1 - \frac{\sigma T_{\text{red}}^4}{IC}$, where σ is the Stefan-Boltzmann constant, $I = 1 \text{ kW/m}^2$ is direct normal irradiation and $C = 5000$ is the solar flux concentration ratio.

The yield and efficiency of thermochemical water splitting by the perovskite $\text{La}_{0.6}\text{Sr}_{0.4}\text{Mn}_{1-y}\text{Cr}_y\text{O}_{3-\delta}$ for reduction at 1773 K and $p\text{O}_2 = 10^{-6} \text{ atm.}$, are plotted as function of composition and oxidation temperature in Figure 7. Equilibrium yields and efficiency is shown in Figures 7a and 7b. For further description and explanation of the efficiency, we plot the input energy $Q_{\text{solar,mat}}$ in Figure 7c and the two most dominant input energy terms, *i.e.* sensible heat for the metal oxide and energy to heat the water to the reaction temperature in Figure 7d. In agreement with the thermodynamic trends, chromium doping plays an influential role on the fuel production, Figure 7a. For the material $\text{La}_{0.6}\text{Sr}_{0.4}\text{MnO}_{3-\delta}$, we observe that a lower oxidation temperature increases the energy output, reaching a maximum of 0.02 mol at 1073 K. Increasing the chromium contents, $y > 0.3$, the trend is entirely different *i.e.* lower oxidation temperature decreases the hydrogen yields.

1 Interestingly, the material with $\text{La}_{0.6}\text{Sr}_{0.4}\text{Mn}_{0.2}\text{Cr}_{0.8}\text{O}_{3-\delta}$ increases its fuel production from
2 0.002 up to 0.011 when the oxidation temperature is increased from 1073-1773K.
3

4 In Figure 7b, it is observed that the solid solution $\text{La}_{0.6}\text{Sr}_{0.4}\text{Mn}_{0.2}\text{Cr}_{0.8}\text{O}_{3-\delta}$ has the highest
5 efficiency of 2.7% for oxidation at 1773 K, which makes this material an interesting
6 candidate for isothermal water and carbon dioxide splitting in comparison to $\text{La}_{0.6}\text{Sr}_{0.4}\text{MnO}_{3-\delta}$
7 which was recently considered as a promising candidate for isothermal water splitting [20].
8 In addition to a higher fuel production and efficiency of $\text{La}_{0.6}\text{Sr}_{0.4}\text{Mn}_{0.2}\text{Cr}_{0.8}\text{O}_{3-\delta}$ this material
9 has displayed improved stability according to earlier studies in related energy technologies
10 [23; 32].
11
12
13
14
15
16
17
18
19
20
21

22 The required input energy $Q_{\text{solar,mat}}$, Figure 7c, decreases for higher oxidation temperature
23 because the sensible heat is lower for a smaller temperature swing as shown in Figure 7d.
24 This explains the relative high efficiency for $y = 0.8$ even though the fuel production is
25 lower. Our computed efficiencies below 3% for $\text{La}_{0.6}\text{Sr}_{0.4}\text{Mn}_{1-y}\text{Cr}_y\text{O}_{3-\delta}$ are related to the
26 water concentration set to one mole of water per one mole of perovskites. It is possible to
27 achieve higher thermal efficiencies using a higher water concentration but this assumes
28 highly efficient heat recuperation [6; 17]. For further discussion of the additional factors that
29 ultimately lowers the efficiency due to an increase in the value of Q_{total} we refer the reader to
30 the work of Jarrett *et al.* [34].
31
32
33
34
35
36
37
38
39
40
41
42
43
44
45
46
47

48 **4 Conclusion**

49

50 We have refined and optimized a Calphad defect model of the $\text{La}_{0.6}\text{Sr}_{0.4}\text{Mn}_{1-y}\text{Cr}_y\text{O}_{3-\delta}$
51 perovskites by including data on $\text{La}_{0.75}\text{Sr}_{0.25}\text{Mn}_{0.5}\text{Cr}_{0.5}\text{O}_{3-\delta}$ from literature between 973 K
52 and 1273 K, to make a predictive thermodynamic assessment of a material previously
53 unexplored for the solar-to-fuel conversion technology. The resulting optimized defect
54 model of the $\text{La}_{1-x}\text{Sr}_x\text{Mn}_{1-y}\text{Cr}_y\text{O}_{3-\delta}$ solution series is used for computations of oxygen
55
56
57
58
59
60
61
62
63
64
65

nonstoichiometry, heat capacity and thermodynamics of the oxygen release reaction in a wide temperature range between 1073K and 1873 K. From this, the following implications on the role of exchange of manganese by chromium can be emphasized: Substituting Mn with Cr on the B-site has two advantages for the solar-to-fuel technology. Firstly, it reduces the heat capacity and secondly it enhances the material's thermodynamic favorability for H₂O and CO₂ splitting near isothermal conditions.

The perovskites reported to this date, are operated thermodynamically favorable in a two-step thermochemical cycle, with a high reduction temperature and low temperature for oxidation. Based on thermodynamic data, we predict that Cr substitution can be utilized to achieve higher efficiency with operation near isothermal conditions. Isothermal or near isothermal solar-to-fuel production comes with operational benefits, such as reduced thermal stress on active and containment materials and it mitigates the energy required to reheat the active material as it cycles between the oxidation and reduction temperature.

The composition La_{0.6}Sr_{0.4}Mn_{0.2}Cr_{0.8}O_{3-δ} reaches a maximum efficiency of 2.7% for isothermal water splitting at 1773 K. The higher efficiency at elevated temperature is related to a strong increase in Δg_{red} . This increase is a direct consequence of a minor decrease of -16% in the enthalpy, Δh_{red} , but a much larger decrease of -58% in entropy Δs_{red} , for a change in chromium content from 0.0 to 0.9. It is possible to achieve efficiencies greater than 2.7% using higher water concentrations, which would assume efficient heat recuperation of unreacted steam or carbon dioxide.

5 Acknowledgements

The authors acknowledge financial support by the ETH Foundation for this work, grant number ETH-05 13-1.

6 Bibliography

- [1] W.C. Chueh, C. Falter, M. Abbott, D. Scipio, P. Furler, S.M. Haile, and A. Steinfeld, *High-flux solar-driven thermochemical dissociation of CO₂ and H₂O using nonstoichiometric ceria*. **Science** 330 (2010) 1797-1801.
- [2] M. Romero, and A. Steinfeld, *Concentrating solar thermal power and thermochemical fuels*. **Energy & Environmental Science** 5 (2012) 9234-9245.
- [3] A.H. McDaniel, E.C. Miller, D. Arifin, A. Ambrosini, E.N. Coker, R. O'Hayre, W.C. Chueh, and J. Tong, *Sr-and Mn-doped LaAlO_{3-δ} for solar thermochemical H₂ and CO production*. **Energy & Environmental Science** 6 (2013) 2424-2428.
- [4] A. Bork, M. Kubicek, M. Struzik, and J. Rupp, *Perovskite La_{0.6}Sr_{0.4}Cr_{1-x}Co_xO_{3-δ} solid solutions for solar-thermochemical fuel production: strategies to lower the operation temperature*. **Journal of Materials Chemistry A** 3 (2015) 15546-15557.
- [5] S. Dey, B. Naidu, A. Govindaraj, and C. Rao, *Noteworthy performance of La_{1-x}Ca_xMnO₃ perovskites in generating H₂ and CO by the thermochemical splitting of H₂O and CO₂*. **Physical Chemistry Chemical Physics** 17 (2015) 122-125.
- [6] J.R. Scheffe, D. Weibel, and A. Steinfeld, *Lanthanum–Strontium–Manganese Perovskites as Redox Materials for Solar Thermochemical Splitting of H₂O and CO₂*. **Energy & Fuels** 27 (2013) 4250-4257.
- [7] H. Schulz, *Short history and present trends of Fischer–Tropsch synthesis*. **Applied Catalysis A: General** 186 (1999) 3-12.
- [8] Q. Jiang, J. Tong, G. Zhou, Z. Jiang, Z. Li, and C. Li, *Thermochemical CO₂ splitting reaction with supported La_xA_{1-x}Fe_yB_{1-y}O₃ (A= Sr, Ce, B= Co, Mn; 0 ≤ x, y ≤ 1) perovskite oxides*. **Solar Energy** 103 (2014) 425-437.
- [9] A. Demont, S. Abanades, and E. Beche, *Investigation of Perovskite Structures as Oxygen-Exchange Redox Materials for Hydrogen Production from Thermochemical Two-Step Water-Splitting Cycles*. **The Journal of Physical Chemistry C** (2014).
- [10] S. Dey, B. Naidu, and C. Rao, *Ln_{0.5}A_{0.5}MnO₃ (Ln= Lanthanide, A= Ca, Sr) Perovskites Exhibiting Remarkable Performance in the Thermochemical Generation of CO and H₂ from CO₂ and H₂O*. **Chemistry-A European Journal** 21 (2015) 7077-7081.
- [11] S.M. Babiniec, E.N. Coker, J.E. Miller, and A. Ambrosini, *Investigation of La_xSr_{1-x}Co_yM_{1-y}O_{3-δ} (M= Mn, Fe) perovskite materials as thermochemical energy storage media*. **Solar Energy** 118 (2015) 451-459.
- [12] A.M. Deml, V. Stevanović, A.M. Holder, M. Sanders, R. O'Hayre, and C.B. Musgrave, *Tunable Oxygen Vacancy Formation Energetics in the Complex Perovskite Oxide Sr_xLa_{1-x}Mn_yAl_{1-y}O₃*. **Chemistry of Materials** 26 (2014) 6595-6602.
- [13] C. Rao, and S. Dey, *Solar thermochemical splitting of water to generate hydrogen*. **Proceedings of the National Academy of Sciences** 114 (2017) 13385-13393.
- [14] M. Takacs, M. Hoes, M. Caduff, T. Cooper, J. Scheffe, and A. Steinfeld, *Oxygen nonstoichiometry, defect equilibria, and thermodynamic characterization of LaMnO₃ perovskites with Ca/Sr A-site and Al B-site doping*. **Acta Materialia** 103 (2016) 700-710.
- [15] C.-K. Yang, Y. Yamazaki, A. Aydin, and S.M. Haile, *Thermodynamic and kinetic assessments of strontium-doped lanthanum manganite perovskites for two-step thermochemical water splitting*. **Journal of Materials Chemistry A** 2 (2014) 13612-13623.
- [16] T. Cooper, J.R. Scheffe, M.E. Galvez, R. Jacot, G. Patzke, and A. Steinfeld, *Lanthanum Manganite Perovskites with Ca/Sr A- site and Al B- site Doping as Effective Oxygen Exchange Materials for Solar Thermochemical Fuel Production*. **Energy Technology** 3 (2015) 1130-1142.
- [17] A.H. Bork, E. Povoden- Karadeniz, and J.L. Rupp, *Modeling Thermochemical Solar- to- Fuel Conversion: CALPHAD for Thermodynamic Assessment Studies of Perovskites, Exemplified for (La, Sr) MnO₃*. **Advanced Energy Materials** (2016).
- [18] P.S. Devi, and M.S. Rao, *Preparation, structure, and properties of strontium-doped lanthanum chromites: La_{1-x}Sr_xCrO₃*. **Journal of Solid State Chemistry** 98 (1992) 237-244.

- [19] M.J. Ignatowich, A.H. Bork, T.C. Davenport, J.L.M. Rupp, C.-K. Yang, Y. Yamazaki, and S.M. Haile, *Thermo-kinetic Limitation in Fuel Production Rates from $\text{La}_{1-x}\text{Sr}_x\text{MnO}_{3-\delta}$ in Thermochemical Cycling* **MRS Communications** 7 (2017) 873-878.
- [20] S. Dey, and C. Rao, *Splitting of CO_2 by manganite perovskites to generate CO by solar isothermal redox cycling*. **ACS Energy Letters** 1 (2016) 237-243.
- [21] I. Al-Shankiti, B.D. Ehrhart, and A.W. Weimer, *Isothermal redox for H_2O and CO_2 splitting—A review and perspective*. **Solar Energy** 156 (2017) 21-29.
- [22] E. Povoden-Karadeniz, M. Chen, T. Ivas, A. Grundy, and L. Gauckler, *Thermodynamic modeling of $\text{La}_2\text{O}_3\text{--SrO--Mn}_2\text{O}_3\text{--Cr}_2\text{O}_3$ for solid oxide fuel cell applications*. **Journal of Materials Research** 27 (2012) 1915-1926.
- [23] S. Tao, J.T. Irvine, and S.M. Plint, *Methane oxidation at redox stable fuel cell electrode $\text{La}_{0.75}\text{Sr}_{0.25}\text{Cr}_{0.5}\text{Mn}_{0.5}\text{O}_{3-\delta}$* . **The Journal of Physical Chemistry B** 110 (2006) 21771-21776.
- [24] M. Oishi, K. Yashiro, K. Sato, J. Mizusaki, and T. Kawada, *Oxygen nonstoichiometry and defect structure analysis of B-site mixed perovskite-type oxide $(\text{La}, \text{Sr})(\text{Cr}, \text{M})\text{O}_{3-\delta}$ ($\text{M} = \text{Ti}, \text{Mn}$ and Fe)*. **Journal of Solid State Chemistry** 181 (2008) 3177-3184.
- [25] W.Z. Zhu, and S. Deevi, *Development of interconnect materials for solid oxide fuel cells*. **Materials Science and Engineering: A** 348 (2003) 227-243.
- [26] M. Hillert, *The compound energy formalism*. **Journal of Alloys and Compounds** 320 (2001) 161-176.
- [27] O. Redlich, and A. Kister, *Algebraic representation of thermodynamic properties and the classification of solutions*. **Industrial & Engineering Chemistry** 40 (1948) 345-348.
- [28] R. Panlener, R. Blumenthal, and J. Garnier, *A thermodynamic study of nonstoichiometric cerium dioxide*. **Journal of Physics and Chemistry of Solids** 36 (1975) 1213-1222.
- [29] J.R. Scheffe, and A. Steinfeld, *Thermodynamic analysis of cerium-based oxides for solar thermochemical fuel production*. **Energy & Fuels** 26 (2012) 1928-1936.
- [30] B. Sundman, B. Jansson, and J.-O. Andersson, *The thermo-calc databank system*. **Calphad** 9 (1985) 153-190.
- [31] M. Zinkevich, D. Djurovic, and F. Aldinger, *Thermodynamic modelling of the cerium–oxygen system*. **Solid State Ionics** 177 (2006) 989-1001.
- [32] T. Nakamura, G. Petzow, and L. Gauckler, *Stability of the perovskite phase LaBO_3 ($\text{B} = \text{V}, \text{Cr}, \text{Mn}, \text{Fe}, \text{Co}, \text{Ni}$) in reducing atmosphere I. Experimental results*. **Materials Research Bulletin** 14 (1979) 649-659.
- [33] A. Steinfeld, *Solar thermochemical production of hydrogen—a review*. **Solar energy** 78 (2005) 603-615.
- [34] C. Jarrett, W. Chueh, C. Yuan, Y. Kawajiri, K.H. Sandhage, and A. Henry, *Critical limitations on the efficiency of two-step thermochemical cycles*. **Solar Energy** 123 (2016) 57-73.

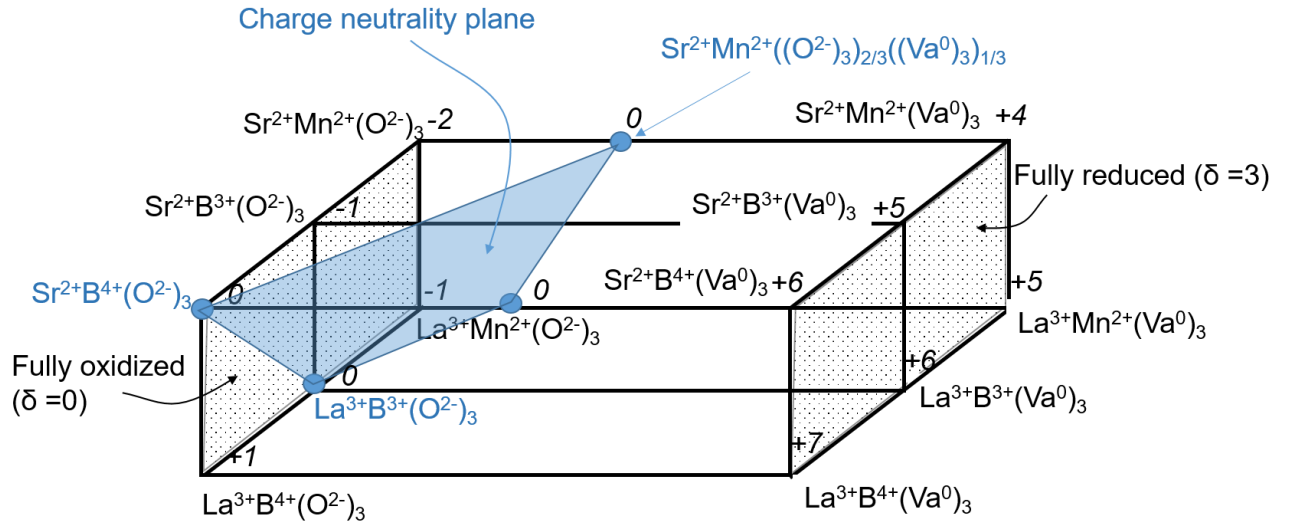


Figure 1. Compositional representation of the perovskite system with the sublattice formula $[\text{La}^{3+}, \text{Sr}^{2+}]^{\text{A}}[\text{Mn}^{2+}, \text{Mn}^{3+}, \text{Mn}^{4+}, \text{Cr}^{3+}, \text{Cr}^{4+}]^{\text{B}}[\text{O}^{2-}, \text{Va}^0]_3$. The charge neutrality plane (blue shaded area) represents all perovskite compositions that are allowed by electroneutrality conditions. Examples of three charge neutral compositions are highlighted in blue: $\text{Sr}^{2+}\text{B}^{4+}(\text{O}^{2-})_3$, $\text{La}^{3+}\text{B}^{3+}(\text{O}^{2-})_3$, $\text{Sr}^{2+}\text{Mn}^{2+}((\text{O}^{2-})_3)_{2/3}((\text{Va}^0)_3)_{1/3}$, where B = Cr or Mn. Fully oxidized to fully reduced ($\delta=3$, purely theoretic oxygen-free) perovskite compounds are highlighted by gray dot shaded area. Examples of charged end-member compositions are shown in black, e.g. $\text{La}^{3+}\text{B}^{4+}(\text{O}^{2-})_3$ and $\text{Sr}^{2+}\text{Mn}^{2+}(\text{Va}^0)_3$ with a charge of +1 and +4 respectively. This representation allows a visualization of potentially realizable compounds obeying charge neutrality.

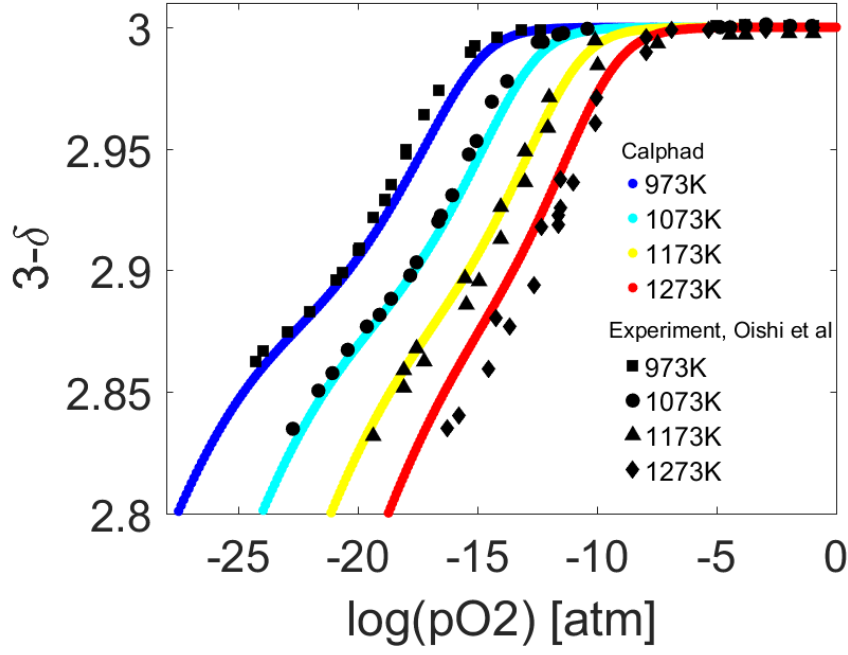
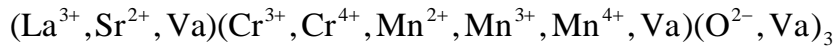


Figure 2: Oxygen nonstoichiometry, δ , of $\text{La}_{0.75}\text{Sr}_{0.25}\text{Cr}_{0.5}\text{Mn}_{0.5}\text{O}_{3-\delta}$ as function of oxygen partial pressure in the temperature range 973K to 1273K. Symbol markers represent data extracted from Oishi et al[1] and colored solid lines correspond to modelled defect chemistry from Calphad.

Table 1. Redlich-Kister parameters for interaction between Cr and Mn on the B-site in the perovskite $\text{La}_{0.6}\text{Sr}_{0.4}\text{Mn}_{1-y}\text{Cr}_y\text{O}_{3-\delta}$.

Optimized Redlich - Kister interaction parameters, J / mol atoms



$${}^0L_{\text{La}^{3+}, \text{Sr}^{2+}: \text{Cr}^{3+}, \text{Mn}^{3+}: \text{O}^{2-}} = -149469$$

$${}^1L_{\text{La}^{3+}, \text{Sr}^{2+}: \text{Cr}^{3+}, \text{Mn}^{3+}: \text{O}^{2-}} = -130631$$

$${}^2L_{\text{La}^{3+}, \text{Sr}^{2+}: \text{Cr}^{3+}, \text{Mn}^{3+}: \text{O}^{2-}} = -109105$$

$${}^0L_{\text{La}^{3+}, \text{Sr}^{2+}: \text{Cr}^{3+}, \text{Mn}^{4+}: \text{O}^{2-}} = -112865$$

$${}^1L_{\text{La}^{3+}, \text{Sr}^{2+}: \text{Cr}^{3+}, \text{Mn}^{4+}: \text{O}^{2-}} = -80494$$

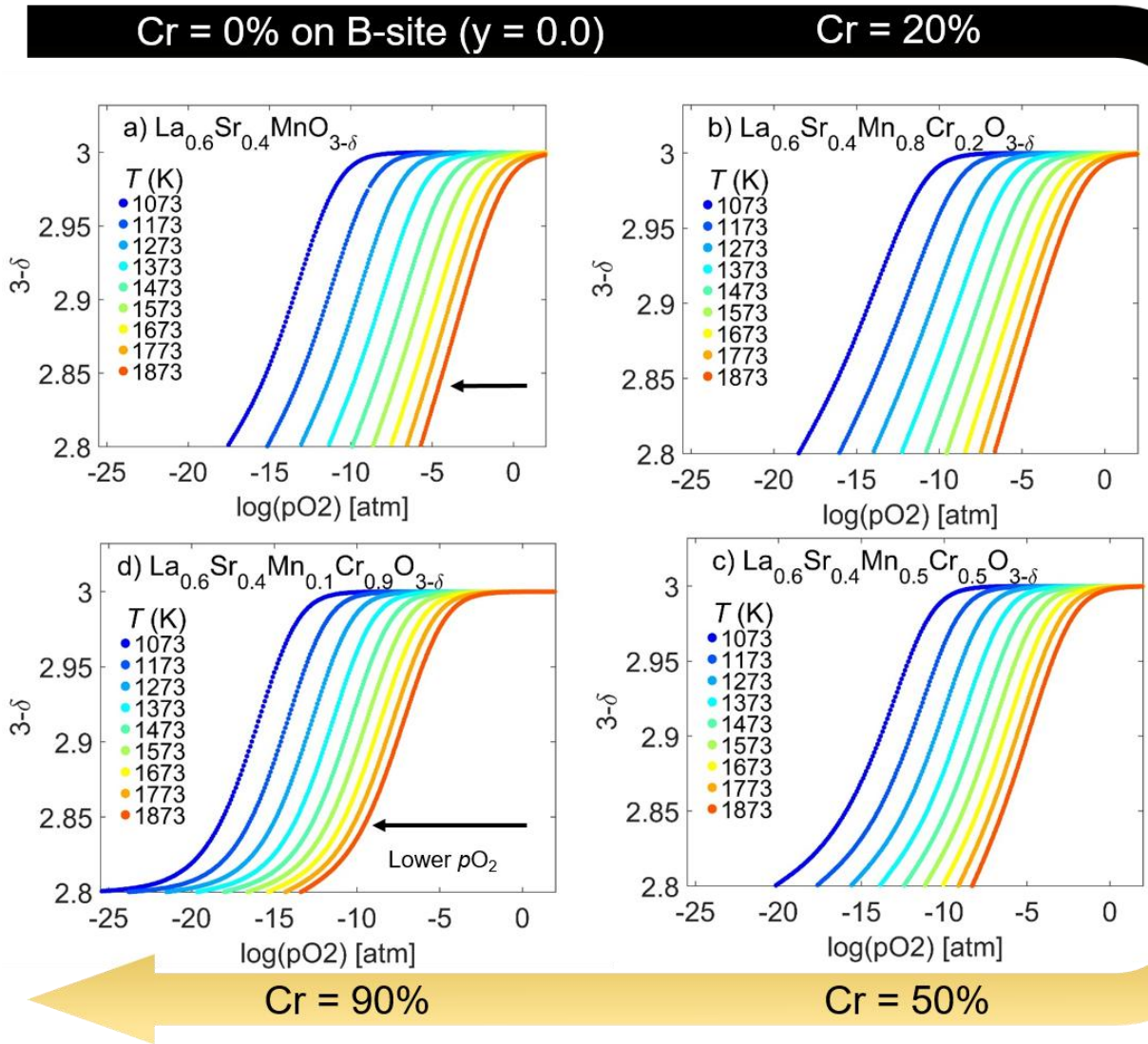


Figure 3. Oxygen nonstoichiometry is shown versus oxygen partial pressure in a temperature window of 1073-1873 K: All data are extracted from CALPHAD libraries with descriptions of defect chemistry of the perovskite solid solutions $La_{0.6}Sr_{0.4}Mn_{1-y}Cr_yO_{3-\delta}$ ($y = 0.0, 0.2, 0.5, 0.9$).

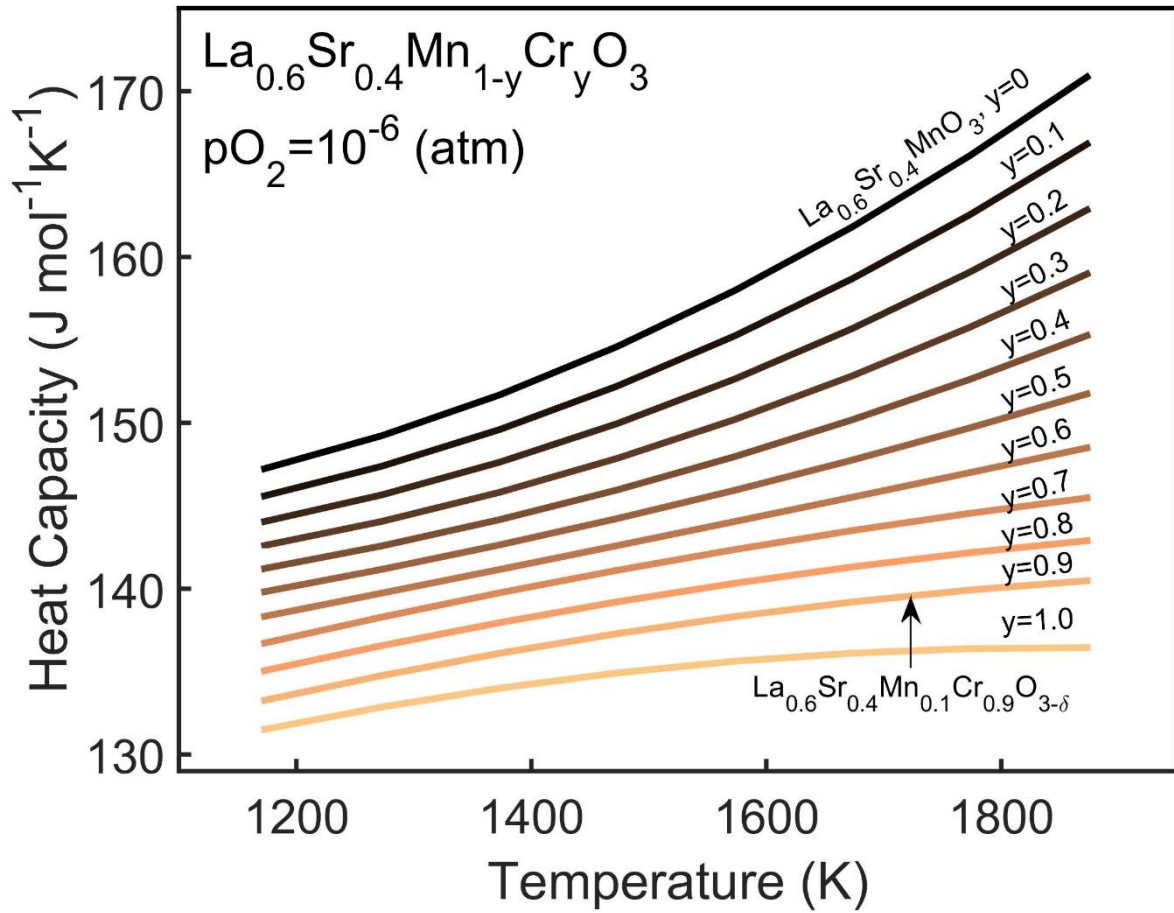
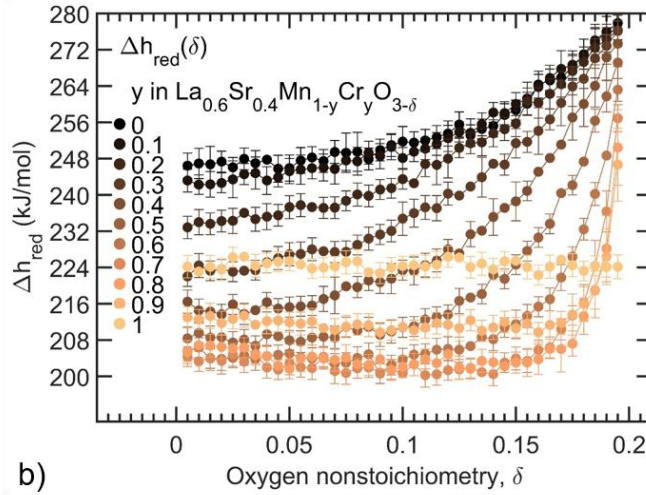
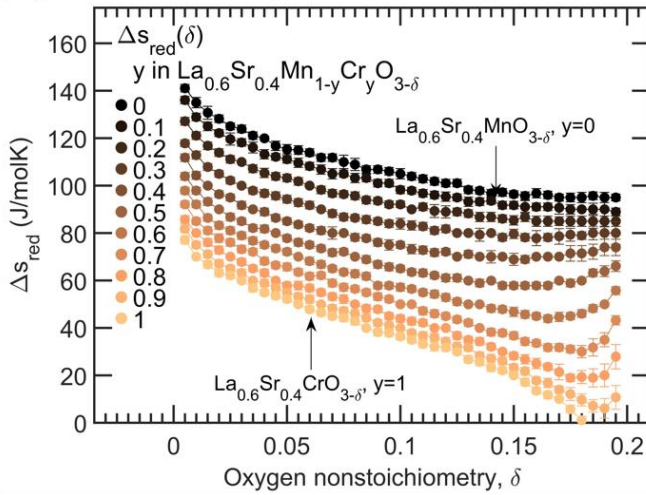


Figure 4. Heat capacity, c_p , as function of temperature of the perovskite oxide $\text{La}_{0.6}\text{Sr}_{0.4}\text{Mn}_{1-y}\text{Cr}_y\text{O}_3$ for ($y= 0.0, 0.1, 0.2, 0.3, 0.4, 0.5, 0.6, 0.7, 0.8, 0.9, 1.0$) compiled from CALPHAD at an oxygen partial pressure of 10^{-6} atm.

a)



b)



c)

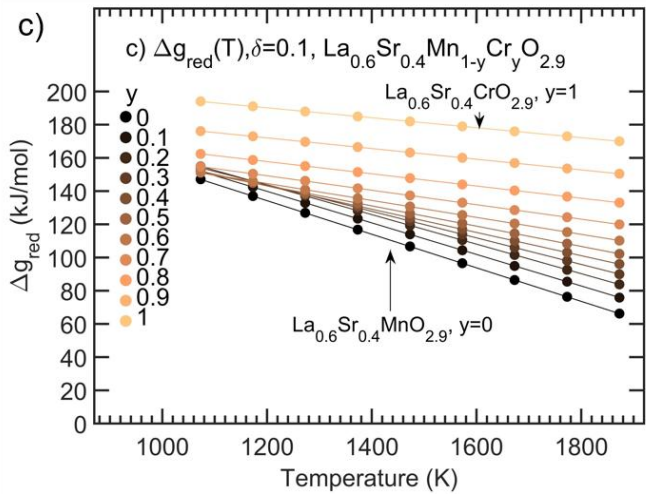


Figure 5. Thermodynamics of the defect reaction $\text{O}_\text{O}^\times + 2\text{Me}_\text{Me}^\times \rightleftharpoons 1/2\text{O}_2(\text{g}) + \text{V}_\text{O}^\bullet + \text{Me}_\text{Me}^\times$ as function of oxygen nonstoichiometry for the solid solutions $\text{La}_{0.6}\text{Sr}_{0.4}\text{Mn}_{1-y}\text{Cr}_y\text{O}_{3-\delta}$ ($y=0, 0.1, 0.2, 0.3, 0.4, 0.5, 0.6, 0.7, 0.8, 0.9, 1.0$): (a) partial molar enthalpy, and (b) partial molar entropy derived from CALPHAD descriptions of oxygen nonstoichiometry versus oxygen partial pressure and temperature. (c) Gibbs free energy change calculated based on the enthalpy and entropy as function of temperature at an oxygen nonstoichiometry of $\delta = 0.1$.

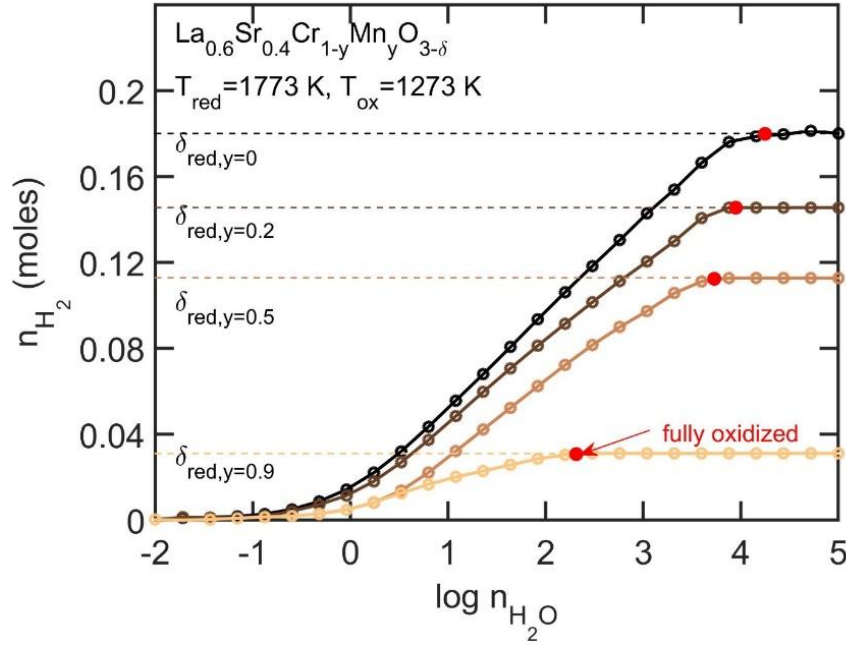


Figure 6. Equilibrium hydrogen fuel yield (n_{H_2}) per mol perovskite plotted as a function of the logarithm of the water concentration n_{H_2O} . Oxidation is carried out at the temperature $T_{ox} = 1273$ K after reduction at the temperature $T_{red} = 1773$ K and $pO_2 = 10^{-6}$ atm., which results in the nonstoichiometries, δ_{red} indicated in the plot for the various compositions $La_{0.6}Sr_{0.4}Mn_{1-y}Cr_yO_3$ ($y = 0.0, 0.2, 0.5, 0.9$). The water concentration is in multiples of mol perovskite n_{ABO_3} .

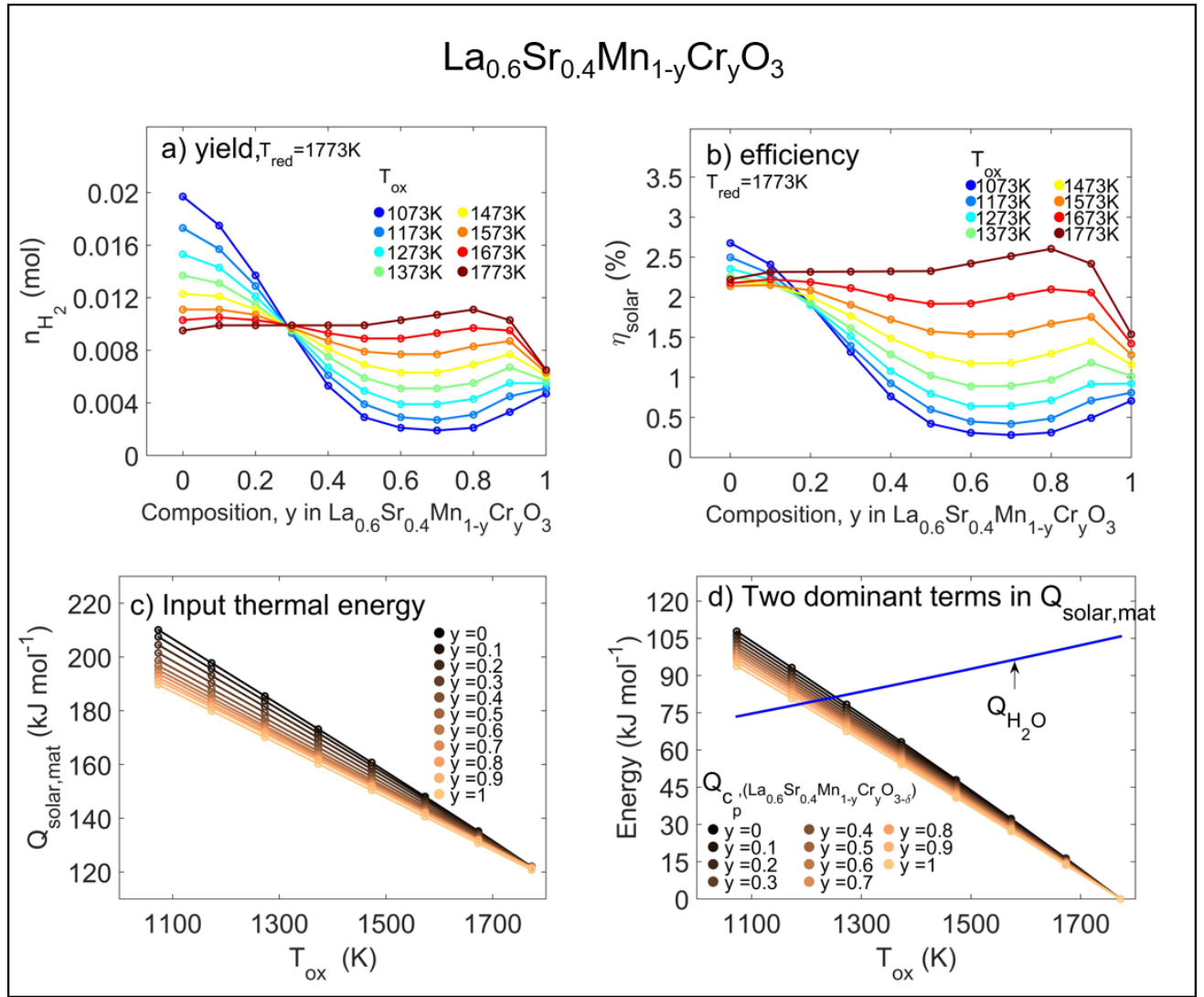


Figure 7. Comparison of yield, efficiency and the input thermal energy for a thermochemical water splitting cycle. Calculated for the entire chromium doping range on the B-site in $\text{La}_{0.6}\text{Sr}_{0.4}\text{Mn}_{1-y}\text{Cr}_y\text{O}_3$ for $y= 0.0, 0.1, 0.2, 0.3, 0.4, 0.5, 0.6, 0.7, 0.8, 0.9, 1.0$. (a) Equilibrium hydrogen yields, n_{H_2} as function of composition and temperature. (b) Efficiency as function of composition and temperature for a water concentration of $n_{\text{H}_2\text{O}} = n_{\text{ABO}_3}$. (c) Material specific solar input, $Q_{\text{solar,mat}}$ to produce the given hydrogen fuel yields. (d) The two most dominant terms in minimum required solar input to $Q_{\text{solar,mat}}$ which is the energy to heat water, $Q_{\text{H}_2\text{O}}$, from room temperature (298 K) to the oxidation temperature T_{ox} and $Q_{\text{cp,}(\text{La}_{0.6}\text{Sr}_{0.4}\text{Mn}_{1-y}\text{Cr}_y\text{O}_3)}$ the sensible heat given by the heat capacity of the metal oxide.

1
2
3
4
5
6
7
8
9
10
11
12
13
14
15
16
17
18
19
20
21
22
23
24
25
26
27
28
29
30
31
32
33
34
35
36
37
38
39
40
41
42
43
44
45
46
47
48
49
50
51
52
53
54
55
56
57
58
59
60
61
62
63
64
65

Bibliography Figures

1. Oishi, M., et al., *Oxygen nonstoichiometry and defect structure analysis of B-site mixed perovskite-type oxide (La, Sr)(Cr, M)O_{3-δ} (M = Ti, Mn and Fe)*. **Journal of Solid State Chemistry**, 2008. 181(11): p. 3177-3184.

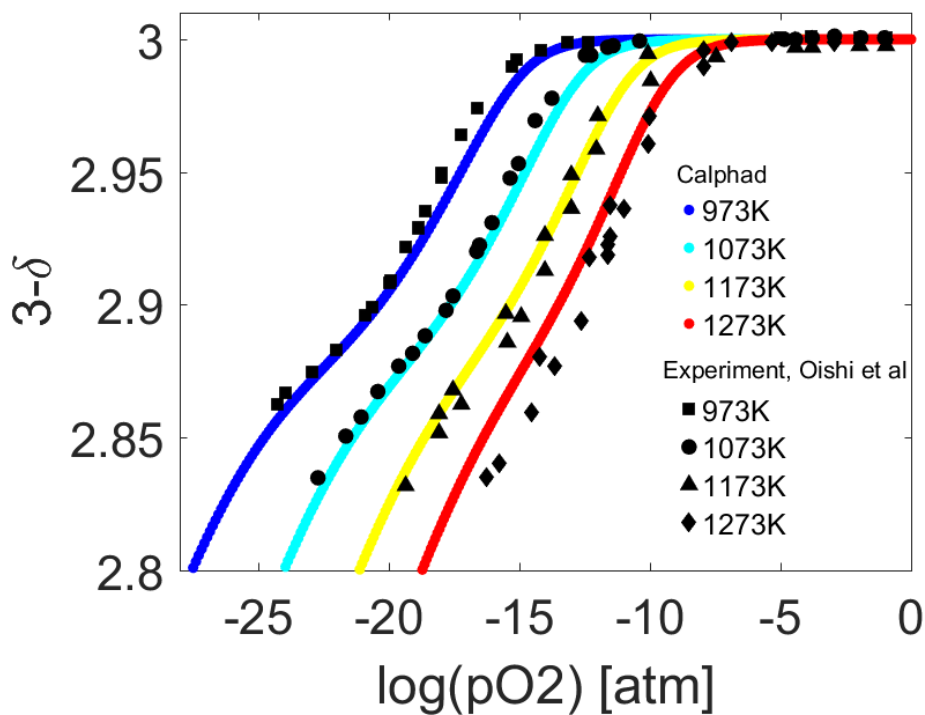
1
2
3
4
5
6
7
8
9
10
11
12
13
14
15
16
17
18
19
20
21
22
23
24
25
26
27
28
29
30
31
32
33
34
35
36
37
38
39
40
41
42
43
44
45
46
47
48
49
50
51
52
53
54
55
56
57
58
59
60
61
62
63
64
65

Supplementary Material

[Click here to download Supplementary Material: Supporting Information.docx](#)

Thermodynamic assessment

Calphad thermochemical description of the perovskite $\text{La}_{0.6}\text{Sr}_{0.4}\text{Mn}_{1-y}\text{Cr}_y\text{O}_{3-\delta}$

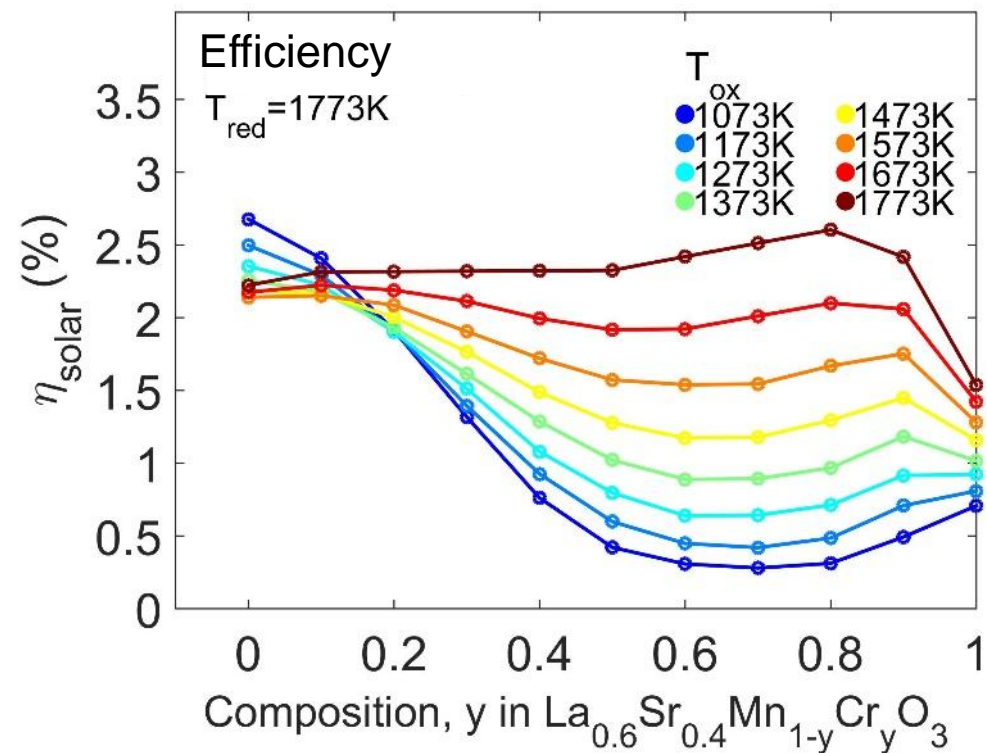


Output: defect chemistry and heat capacity

Model

Prediction: Solar-to-fuel Performance

Cr-substitution in $\text{La}_{0.6}\text{Sr}_{0.4}\text{Mn}_{1-y}\text{Cr}_y\text{O}_3$ is beneficial near isothermal conditions



Output: fuel production and efficiency